Ghost-free high dynamic range imaging — Source link ⬈

Yong Seok Heo, Kyoung Mu Lee, Sang Uk Lee, Young-Su Moon ...+1 more authors

Institutions: Seoul National University, Samsung

Published on: 08 Nov 2010 - Asian Conference on Computer Vision

Topics: HDRi and High-dynamic-range imaging

Related papers:

- Recovering high dynamic range radiance maps from photographs

- Artifact-free High Dynamic Range imaging

- Automatic High-Dynamic Range Image Generation for Dynamic Scenes

- Robust patch-based hdr reconstruction of dynamic scenes

- Ghost Removal in High Dynamic Range Images

Ghost-Free High Dynamic Range Imaging

Yong Seok Heo[1], Kyoung Mu Lee[1], Sang Uk Lee[1],
Youngsu Moon[2], and Joonhyuk Cha[2]

[1] Department of EECS, ASRI, Seoul National University, Seoul, Korea
http://cv.snu.ac.kr
[2] Samsung Advanced Institute of Technology, Samsung Electronics Co.,
Yong-In, Korea

Abstract. Most high dynamic range image (HDRI) algorithms assume stationary scene for registering multiple images which are taken under different exposure settings. In practice, however, there can be some global or local movements between images caused by either camera or object motions. This situation usually causes ghost artifacts which make the same object appear multiple times in the resultant HDRI. To solve this problem, most conventional algorithms conduct ghost detection procedures followed by ghost region filling with the estimated radiance values. However, usually these methods largely depend on the accuracy of the ghost detection results, and thus often suffer from color artifacts around the ghost regions. In this paper, we propose a new robust ghost-free HDRI generation algorithm that does not require accurate ghost detection and not suffer from the color artifact problem. To deal with the ghost problem, our algorithm utilizes the global intensity transfer functions obtained from joint probability density functions (pdfs) between different exposure images. Then, to estimate reliable radiance values, we employ a generalized weighted filtering technique using the global intensity transfer functions. Experimental results show that our method produces the state-of-the-art performance in generating ghost-free HDR images.

1 Introduction

Typical cameras represent a pixel using only 256 values for each of the red, green, and blue channel. On the contrary, the range of radiance of a real scene has a far wider range than 256 values [1]. Hence, a photograph taken by a conventional camera can not capture the whole dynamic range of scene radiance. So, the cameras usually compress the scene radiance value using a proper function which is often called the camera response function (CRF). This process, however, can cause unpleasant under- or over-exposed regions.

Many approaches have been proposed to recover a high dynamic range image (HDRI) by estimating the CRF using multiple low dynamic range images (LDRIs) which are taken under different exposure settings for the scene [2–5].

The pioneering work of Mann and Picard [2] used a gamma function to estimate a CRF. Debevec and Malik [3] estimated a CRF using error function with smoothness constraint in a least squared-error sense, and then the radiance value of each pixel is determined by a weighted sum of the radiance values of multiple exposure images. Mitsunaga and Nayar [4] approximated a CRF using a polynomial with a fixed degree. They only assumed that the ratios of the exposures between images are roughly known, instead of the exposure time. Grossberg and Nayar [5] suggested a robust method to recover a CRF using intensity histograms instead of a pixel value itself without image registration.

In practice, however, while fusing multiple images into a single radiance image, all these methods severely suffer from artifacts caused by moving camera and/or objects, because they assume a stationary scene. A camera motion causes global image transformation such as an affine or perspective transformations between different exposure images. If one takes photographs using a tripod, this problem might be reduced. A more critical problem, however, is caused by an object motion which invokes inevitable ghost artifacts that make the same object appears multiple times in a generated HDRI. Due to these reasons, practically it is a very important and critical issue to produce a ghost-free HDRI from multiple images.

In this paper, we propose a new HDRI generation method that is very effective for handling global and local movements from multiple exposures. Fig. 1 shows an example of our HDRI generated from multiple LDRIs with object motions. Compared with the standard method [3], our proposed method produces much clear and ghost-free HDRI.

| (a) | (b) | (c) | (d) |

| (e) | (f) |
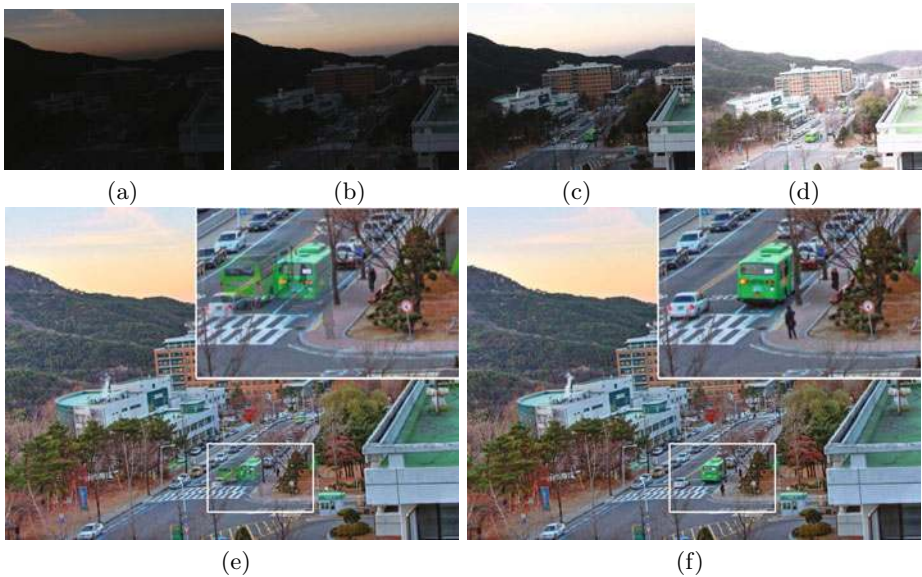
Fig. 1. (a)-(d) are input LDRIs. (e) Result of the standard HDRI method [3]. (f) Result of the proposed method.

2   Previous Works

There are several works for handling ghost artifacts for HDRI generation. Jacobs *et. al.* [6] compared two measures to detect ghost regions such as variance image (VI) [1] and uncertainty image (UI) [6]. They argued that VI was effective for detecting high contrast movement such as moving people, cars, and etc., while UI was effective for low contrast movement such as moving leaves and water rippling [6]. Grosch [7] detected ghost regions using predicted pixel colors which were estimated from the CRF. They defined an error map that had invalid pixel set by thresholding the absolute difference value between the predicted pixel color and the original color. However, These methods have a common drawback that the ghost detection results tend to be sensitive to the threshold values of those measures. Also, they can decrease the dynamic range of ghost regions, since they fill the detected ghost regions with the radiance values from only a single image.

Some other approaches utilize as many multiple exposures as possible for ghost regions. Gallo *et. al.* [8] detected ghost pixels using a linear property of log radiance values in block-wise comparison. For each pixel, they combined multiple exposures except for the images that had ghost regions. Then, they blended the block boundaries to reduce the color difference between neighboring blocks. Raman *et. al.* [9] suggested a similar approach. They also detected ghost regions using block-based comparison between different exposures followed by thresholding. Then, they performed the Poisson blending between neighboring blocks. However, these methods still suffer from color artifacts around block boundaries due to inaccurate CRF estimation [8].

Alternatively, there are other approaches that solve this problem by adjusting weighting function in the Debevec and Malik's weighted average framework [3]. Khan *et. al.* [10] suggested a ghost removal method by adjusting weights when combining multiple exposures. They assumed that all pixels were belonging to either foreground (moving part) or background (static part), and those background pixels were significantly prevailed than the pixels of foreground moving objects. Their weight function is composed of two terms regarding the probability of being correctly exposed and the probability of belonging to the background. Then, they iteratively updated the probability of belonging to the background. Pedone and Heikkilä [11] suggested a similar approach to [10]. They estimated bandwidth matrices for computing the accurate probability of belonging to the background, and propagated the influence of the low probabilities to the surrounding regions using an energy minimization technique. A main drawback of these methods is that if the object of interest is moving, that object can be recognized as ghost and disappeared in the resultant HDRI.

On the other hand, Bogoni [12] estimated motion vectors using optical flow for different exposure images, and then used those information to warp other exposure images. Kang *et. al.* [13] also used a gradient-based optical flow method to find corresponding pixels between neighboring images that had alternating different exposures for producing HDR video sequences. However, it is not trivial to find the accurate correspondence between different exposure images.
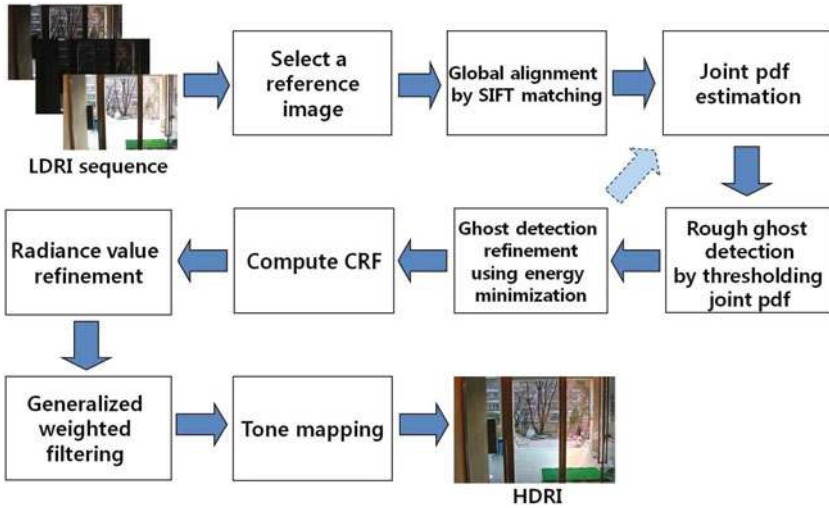
Fig. 2. An overview of our approach

Most approaches described above determine whether a pixel in each image is a ghost or not in deterministic or statistical manners. Then, to compute the radiance values, they utilize the un-ghost pixels of multiple exposures only in the same position. In this case, when ghost detection is not so accurate enough, many artifacts arise in the resultant HDRI. Also, even when the ghost detection is acceptable, it is still problematic to fill those regions with proper radiance values. Filling those regions using only a single exposure image can reduce the dynamic range, and also filling them using only un-ghost pixels can produce color artifacts around the ghost regions due to the inaccurate CRF estimation.

3   Proposed Algorithm

Fig. 2 shows an overview of our algorithm. First, we select a reference image to generate a HDRI among multiple exposure images. Then, we globally align other images to this reference image to handle camera motions caused by handshakes. Next, we estimate the joint probability density functions (pdfs) between the reference image and other images to estimate the global intensity transfer functions. Based on these joint pdfs, we roughly detect ghost regions in other images w.r.t. the reference image. Then, a refinement procedure is followed based on a global energy minimization framework using Graph-cuts [14]. The joint pdf and ghost detection processes are performed recursively for two or three steps. After that, we compute a CRF by sampling some un-ghost pixels. Based on this CRF, we refine the radiance values of other images w.r.t. that of the reference image to reduce the CRF estimation error. Finally, using the refined radiance

values and the global intensity transfer functions of all exposure images, we perform a generalized weighted filtering to compute the final radiance values. After tone-mapping process, we produce a ghost-free HDRI for the reference image. Detailed explanation is as follows.

3.1   Reference Image Selection and Global Image Alignment

First, we have to select a reference image among multiple exposure images. We choose the image that has least saturated regions such as under- or over-exposed regions as the reference image. Then, we globally align other images to this reference image. In this global alignment, we use SIFT feature-based alignment method [15], since SIFT descriptor is robust to exposure changes [15] and it can handle affine or perspective image transformations in some degree. After finding SIFT features, we compute homographies based on these features using RANSAC [16], and then warp other images to the reference image. However, even after this global alignment, there still remain some local misalignments due to moving objects that usually cause ghost artifacts. Let us describe how to deal with this problem in detail in the following sections.

3.2   Joint Pdf Estimation

To deal with ghost artifacts, we need a measure to judge the correspondence between different exposure images. For this measure, we use a global intensity relationship [17]. To estimate the global relationship between different exposures, we construct a joint histogram $P_{n_0,n}^k$ for each color channel $k \in \{R, G, B\}$ between the reference n_0^{th} image and other n^{th} image. $P_{n_0,n}^k$ is defined by

$$P_{n_0,n}^k(i,j) = \frac{1}{M} \sum_p G_n(p) \cdot T[(i,j) = (I_{n_0}^k(p), I_n^k(p))], \qquad (1)$$

where p is a pixel position index. $T[\cdot]$ is one if the argument is true, zero otherwise. M is the total number of corresponding pixels in an image. $I_n^k(\cdot)$ is an intensity value of k channel of nth image. $G_n(\cdot)$ is a ghost weight function which is defined in the following section. At first iteration, we set $G_n(\cdot) = 1$ for all pixels of all exposures. Next, Parzen windowing is performed by convolving 2D Gaussian function to have smooth joint pdfs. In this work, we used a 5×5 Gaussian function. Then, we normalize the joint histograms such that the sum of all the elements equals to one. Examples of joint pdfs are shown in Fig. 3 (d)-(f) for the images in Fig. 3 (a)-(c), where (a) is the reference image.

3.3   Ghost Region Estimation

For each nth image except for the reference image, we detect ghost pixels by defining ghost weight $G_n(\cdot)$ which is defined by

(a) Image 1   (b) Image 2   (c) Image 3

(d) $P_{1,1}^G$ (e) $P_{1,2}^G$ (f) $P_{1,3}^G$
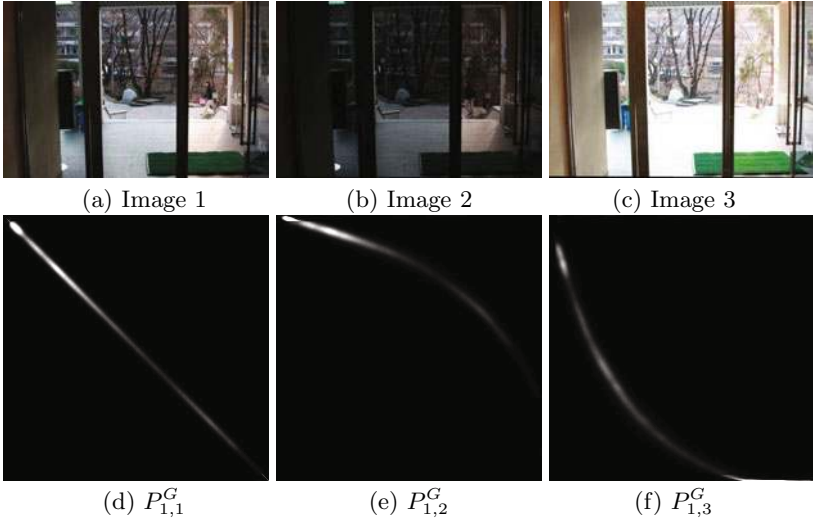
Fig. 3. (a)-(c) are input image sequence, where (a) is the reference image. (d)-(f) are joint pdfs of the green channel corresponding to (a)-(c), respectively.

$$G_n(p) = \begin{cases} 0, \; if \; P_{n_0,n}^R(I_{n_0}^R(p), I_n^R(p)) < c \; or \\ \qquad P_{n_0,n}^G(I_{n_0}^G(p), I_n^G(p)) < c \; or \\ \qquad P_{n_0,n}^B(I_{n_0}^B(p), I_n^B(p)) < c \\ 1, \; otherwise \end{cases} . \qquad (2)$$

$G_n(p) = 0$ represents that a pixel p in the nth image is a ghost, while $G_n(p) = 1$ represents that the pixel p is a non-ghost pixel. For the reference image, all the pixels are assumed to be non-ghost pixels. In this work, we set the threshold c as 10^{-5}. These ghost regions initially determined by thresholding joint pdfs could be very noisy and inaccurate. Hence, we refine the ghost detection result by using an energy minimization approach. For each image, we define the total energy to minimize as follows:

$$E(f_n) = \sum_p D_p(f_n(p)) + \sum_p \sum_{q \in N(p)} V_{pq}(f_n(p), f_n(q)), \qquad (3)$$

where the Boolean label $f_n \in \{0,1\}$ represents whether a pixel is a ghost or not. When $f_n(p) = 0$, a pixel p in the nth image is a ghost, while $f_n(p) = 1$ represents that a pixel p in the nth image is not a ghost pixel. $N(p)$ represents a neighboring pixels of p. In this work, we use a four-neighborhood system. Our data cost $D_p(\cdot)$ is defined by

$$D_p(f_n(p)) = \begin{cases} 0, \; if \; (f_n(p) = 0 \land G_n(p) = 0) \; or \\ \qquad (f_n(p) = 1 \land G_n(p) = 1) \\ \beta, \; otherwise \end{cases} , \qquad (4)$$

(a)   (b)   (c)   (d)
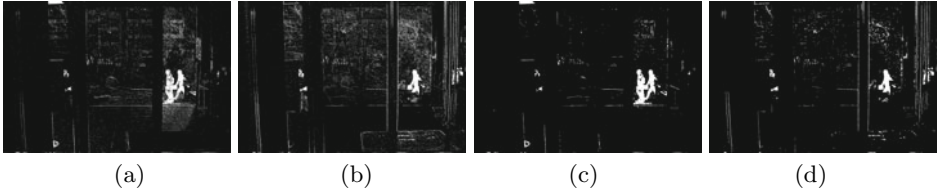
Fig. 4. Ghost detection result. Image 1 (in Fig. 3 (a)) is the reference image. (a) and (b) are the ghost regions corresponding to image 2 and image 3, respectively, using thresholding joint pdf. (c) and (d) are the refined ghost regions corresponding to image 2 and image 3, respectively, using global energy minimization.

where β is a constant, which we set as $\beta = 2.5$. We define a smoothness cost $V_{pq}(\cdot, \cdot)$ as a truncated linear function defined by

$$V_{pq}(f_n(p), f_n(q)) = \lambda_{pq} \cdot \min(|f_n(p) - f_n(q)|, V_{\max}),$$
$$\lambda_{pq} = \begin{cases} \lambda_L, & \begin{aligned} if \, \{(&|\mathrm{I}_{n_0}(p) - \mathrm{I}_{n_0}(q)| < \eta) \vee \\ (&|\mathrm{I}_n(p) - \mathrm{I}_n(q)| < \eta)\} \end{aligned} \\ \lambda_S, & otherwise \end{cases}, \qquad (5)$$

where $\lambda_L > \lambda_S$, and $\mathrm{I}_n(p)$ represents a gray value of a pixel p in the nth image. Note that the strength of $V_{pq}(\cdot, \cdot)$ depends on the intensity difference. If the intensity change between neighboring pixels is smaller than the threshold η, we emphasize more smoothness by choosing a larger λ_L value than a smaller one, λ_S. In this work, we set variables in Eq. (5) as follows: $V_{\max} = 1$, $\eta = 5$, $\lambda_L = 3.0$, $\lambda_S = 1.0$. The total energy $E(f_n)$ is optimized using the Graph-cuts (alpha-expansion) algorithm [14]. Using optimized $f_n(\cdot)$, $G_n(\cdot)$ is also updated. Estimating joint pdf and ghost detection processes are iteratively updated. Empirically, two or three iterations are sufficient for convergence.

A ghost estimation example for Fig. 3 (a)-(c) is shown in Fig. 4, where white pixels represent the ghost pixels. We can clearly see that, after global energy minimization, ghost detection results become less noisy and more accurate than those of naive thresholding. Also, it is worth noting that our method does not directly use these ghost detection results, since these results can be still errorneous. Instead, we apply more robust filtering method, which is described in section 3.5.

3.4   Camera Response Function Estimation and Radiance Value Refinement

If we assume that exposure time Δt_n is known, the radiance value of a pixel p in the nth image can be obtained [3] by

$$\ln E_n^k(p) = g(I_n^k(p)) - \ln \Delta t_n, \qquad (6)$$

where E represents a radiance value and $g(\cdot)$ is an inverse camera response function. Note that our actual goal is to compute the radiance values for all the pixels in the reference image. Hence, to estimate the radiance value, we should estimate the inverse CRF function $g(\cdot)$.

To compute $g(\cdot)$, we randomly sample a number of points (55 in this work), avoiding ghost regions and edge regions. Then, we computed $g(\cdot)$ using the method [3]. Also, as [3] suggested, combined radiance value is computed as a weighted average as follows:

$$\ln E^k(p) = \frac{\sum\limits_{n} w(I_n^k(p))(g(I_n^k(p) - \ln \Delta t_n))}{\sum\limits_{n} w(I_n^k(p))}, \qquad (7)$$

where $w(\cdot)$ is a triangle-shaped function defined by

$$w(z) = \begin{cases} z - z_{\min} \ for \ z \leq 0.5(z_{\min} + z_{\max}) \\ z_{\max} - z \ for \ z > 0.5(z_{\min} + z_{\max}) \end{cases}, \qquad (8)$$

where $z_{\min}$ and $z_{\max}$ are the minimum and maximum intensity values, respectively.

To eliminate ghost artifacts, we should combine a set of exposure images which does not include ghost pixels in calculating Eq. (7). However, even if we accurately detect ghost pixels, there can be still significant color artifacts due to inaccurate CRF estimation [8]. In other words, averaging from different sets of exposure images which do not include ghost pixels often induces significant color differences, because each E value of the same position for different exposure images could have different values owing to inaccurate $g(\cdot)$.

The estimated CRF can be inaccurate by various factors such as inaccurate ghost detection, image alignment error, noise and blurring. To solve this problem, we refine the radiance values of other images such that all the pixels of different exposure images have consistent radiance values to the reference image. First, for non-ghost pixels, we compute the radiance values using Eq. (7). Then, we obtain refined radiance value $\bar{E}_n^k(\cdot)$ by averaging the radiance values for each exposure images as follows:

$$\ln \bar{E}_n^k(z) = \frac{1}{C} \sum_{p, \, I_n^k(p)=z} G_n(p) \cdot \ln E^k(p), \qquad (9)$$

where C is a normalization constant. To acquire more smooth curve, we can adopt a more sophisticated curve-fitting algorithm [4].

3.5   Generalized Weighted Filtering Method

In this section, we propose a robust weighted filtering approach for HDRI generation. Fig. 5 depicts our generalized weighted filtering scheme. First, using the estimated joint pdf, the global intensity transfer function between the reference n_0^{th} image and the nth image can be computed in the minimum mean squared error (MMSE) sense. To consider the saturated cases, we define the global intensity transfer functions according to the exposure time of images as follows:
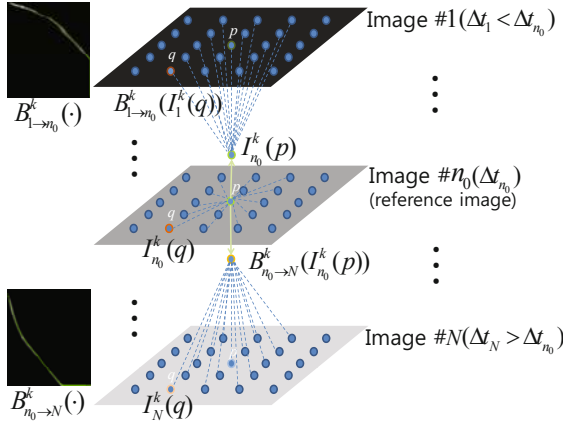
Fig. 5. Generalized weighted filtering scheme. The number of input images is N. Input images are aligned according to exposure time. The final radiance value $\hat{E}$ of the reference n_0^{th} image is computed using weighted sum of refined radiance values $\bar{E}_n$ of images. For each pixel q of nth image in the window $L(p)$ centered at pixel p, the total weight is determined by combining three weights; properly exposed weight $w(\cdot)$, geometric distance weight $d(p, q)$, and color difference weight $c_{n_0,n}(p, q)$.

$$
\begin{aligned}
B_{n_0 \to n}^k(i) &= \frac{\sum\limits_{j=0}^{255} P_{n_0,n}^k(i,j) \cdot j}{\sum\limits_{j=0}^{255} P_{n_0,n}^k(i,j)} \quad (for\ \Delta t_{n_0} < \Delta t_n), \\
B_{n \to n_0}^k(j) &= \frac{\sum\limits_{i=0}^{255} P_{n_0,n}^k(i,j) \cdot i}{\sum\limits_{i=0}^{255} P_{n_0,n}^k(i,j)} \quad (for\ \Delta t_{n_0} \geq \Delta t_n).
\end{aligned}
\tag{10}
$$

For a pixel p in the reference image, we define a window region $L(p)$ that includes all the pixels around the center pixel p in all the exposure images. Then, to compute the final radiance value $\hat{E}^k(\cdot)$, we compute a weighted sum based on the bilateral filtering weight [18] and the intensity weight as follows:

$$
\begin{aligned}
\ln \hat{E}^k(p) &= \frac{\sum\limits_n \sum\limits_{q \in L(p)} w(I_n^k(q)) c_{n_0,n}(p,q) d(p,q) \ln \bar{E}_n^k(I_n^k(q))}{\sum\limits_n \sum\limits_{q \in L(p)} w(I_n^k(q)) c_{n_0,n}(p,q) d(p,q)}, \\
c_{n_0,n}(p,q) &= \exp\left(\frac{-\sum\limits_k \psi_{n_0,n}^k(p,q)}{\sigma_c^2} \right), \\
\psi_{n_0,n}^k(p,q) &= \begin{cases} \left| B_{n_0 \to n}^k(I_{n_0}^k(p)) - I_n^k(q) \right|^2 & (for\ \Delta t_{n_0} < \Delta t_n) \\ \left| I_{n_0}^k(p) - B_{n \to n_0}^k(I_n^k(q)) \right|^2 & (for\ \Delta t_{n_0} \geq \Delta t_n) \end{cases}, \\
d(p,q) &= \exp\left(\frac{-\|p-q\|^2}{\sigma_d^2} \right),
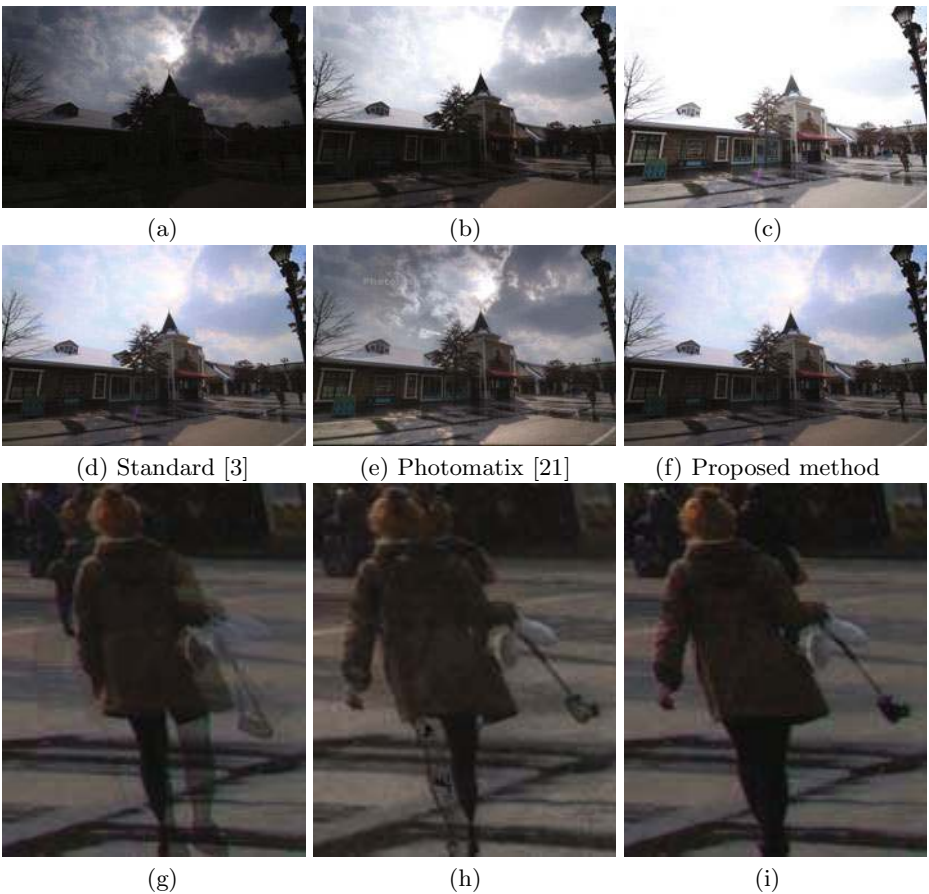\end{aligned}
\tag{11}
$$
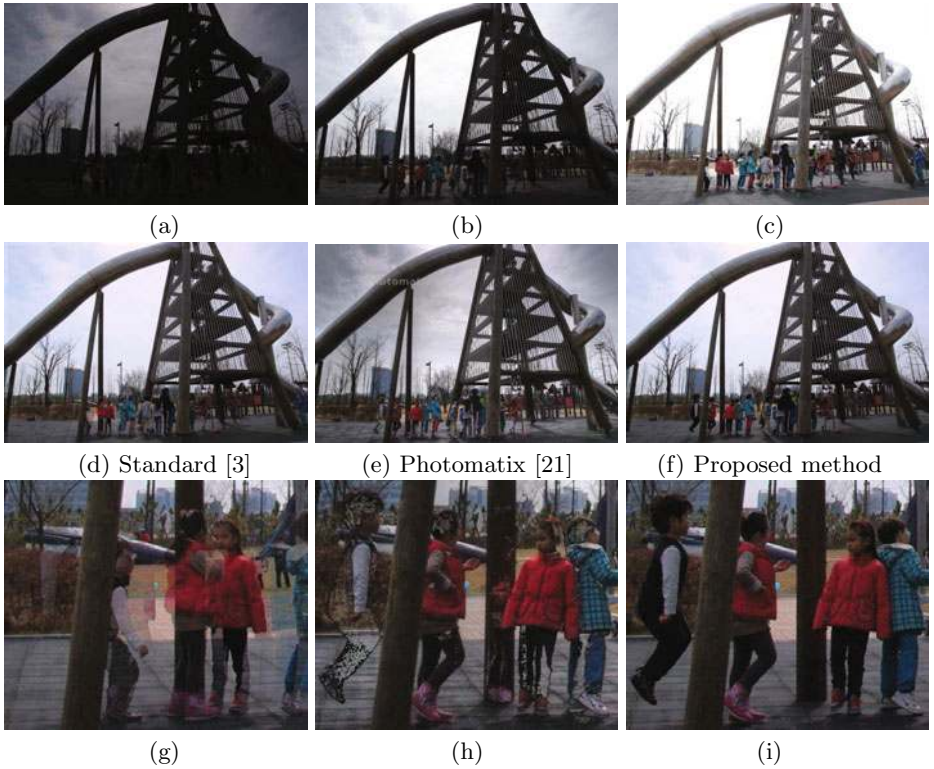
Fig. 6. Playground sequence. (a)-(c) are input LDR images, where (b) is the reference image. (d) Result of the standard method [3]. (e) Result of the Photomatix [21]. (f) Result of the proposed method. (g)-(i) are the magnified views of (d)-(f), respectively.

where $w(\cdot)$ is defined in Eq. (8) that emphasizes properly exposed intensity. $c_{n_0,n}(\cdot,\cdot)$ is a weighting function for color difference between two pixels, $d(\cdot,\cdot)$ is a weighting function for geometric distance between two pixels, and $\|\cdot\|$ represents the Euclidean distance. Note that, in Eq. (11), we use the refined radiance values $\bar{E}_n^k(\cdot)$ in Eq. (9) instead of the radiance values from the estimated CRF function, because the refined radiance values produce less color artifacts when combining radiance values of multiple exposures. Also, in order to compute $c_{n_0,n}(\cdot,\cdot)$, using the global intensity transfer functions in Eq. (10) the intensity of the reference n_0^{th} image is transformed to n^{th} image that has longer exposure time than that of the n_0^{th} image. Conversely, for n^{th} image that has shorter exposure time than that of n_0^{th} image, the intensity of nth image is transformed to the n_0^{th} image. This weighted filtering approach can be considered as a generalized Debevec & Malik approach [3] in that it considers a wider range of pixels, and is robust to ghost artifacts, image misalignments and CRF estimation error. In this work, we set variables in Eq. (11) as $\sigma_c = 7$, $\sigma_d = 10$. The size of $L(p)$ was set as 21×21 for each exposure image.

4   Experimental Results

To evaluate the performance of our method, we tested our algorithm for various scenes that include camera and object movements. To visualize computed radiance values, we averaged the results of both gradient-based [19] and photographic [20] tone-mapping methods.

First, we compared our method with the commercial Photomatix software [21]. For Photomatix software, we tried to reduce ghost artifacts with 'moving objects/people' and 'high' detection modes. Fig. 6 and 7 (a)-(c) are the input images taken by a Pentax K-7 camera with exposure bracketing mode of three exposures (-2EV, 0EV, 2EV). In Fig. 6 and 7, (d)-(f) are the results of the

(a)   (b)   (c)

(d) Standard [3]   (e) Photomatix [21]   (f) Proposed method

(g)   (h)   (i)

Fig. 7. Amusement park sequence. (a)-(c) are input LDR images, where (b) is the reference image. (d) Result of the standard method [3]. (e) Result of the Photomatix [21]. (f) Result of the proposed method. (g)-(i) are the magnified views of (d)-(f), respectively.

(a)   (b)   (c)   (d)   (e)

(f) Standard [3]   (g) Gallo *et. al.* [8]   (h) Proposed method

(i)   (j)
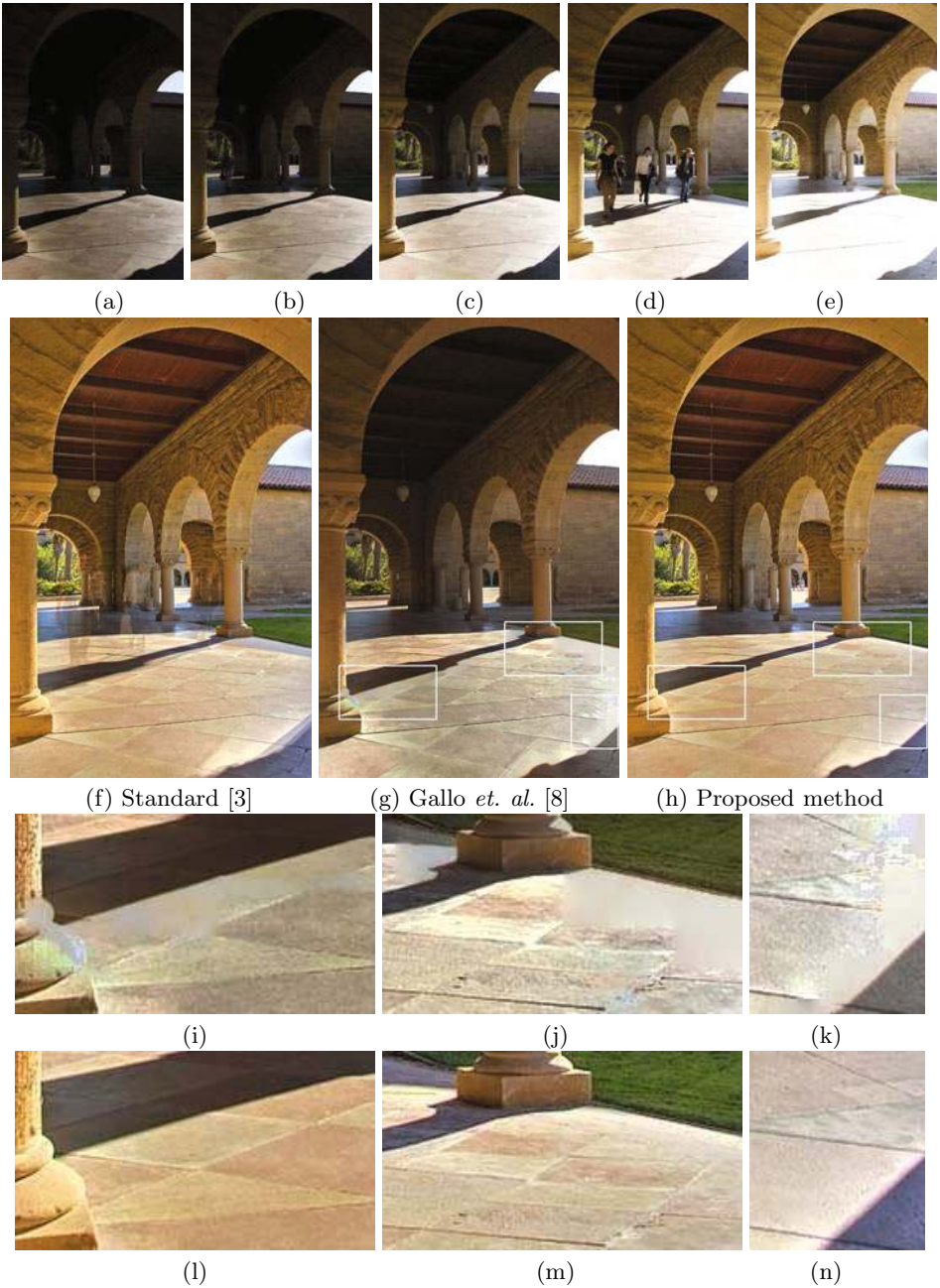

(k)   (l)
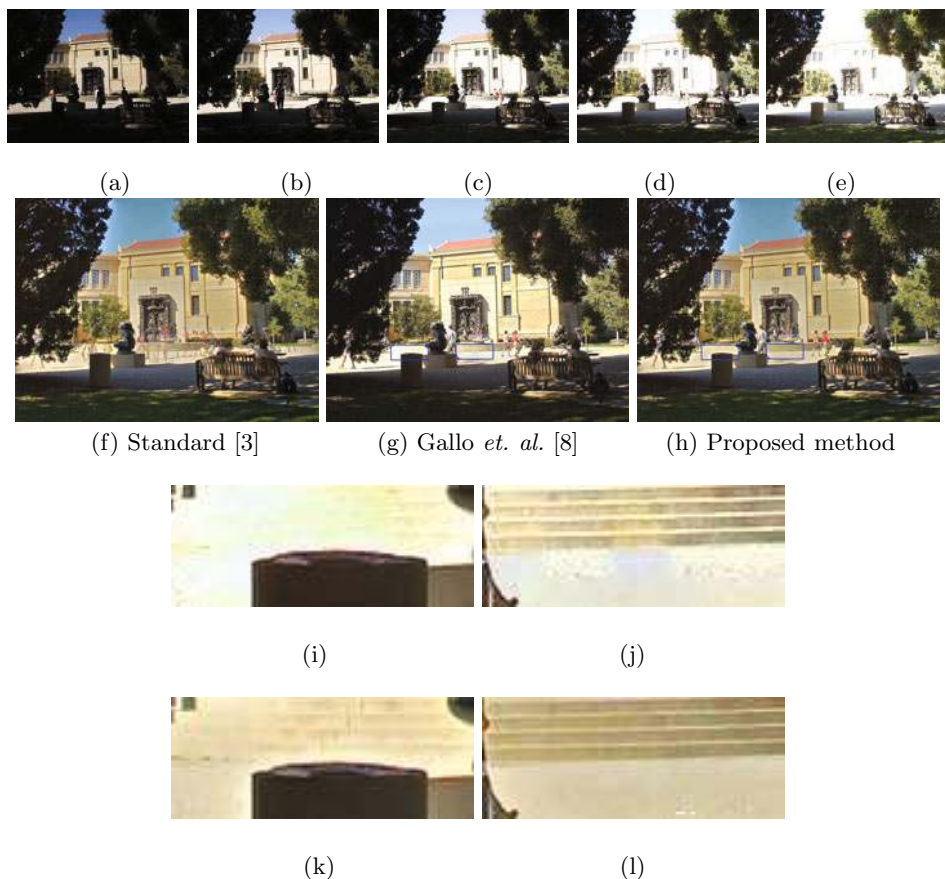
Fig. 8. Sculpture garden sequence. (a)-(e) are input LDR images, where (c) is the reference image. (f) Result of the standard method [3]. (g) Result of [8]. (h) Result of the proposed method. (i)-(j) are the magnified views of the blue rectangle regions in (g). (k)-(l) are the magnified views of the blue rectangle regions in (h).

standard method [3], the Photomatix [21], and the proposed method, respectively. For local movement regions, magnified views of (d)-(f) are shown in (g)-(i), respectively. As expected, we can observe that there are severe ghost artifacts in the standard method. Although the Photomatix reduces ghost artifacts a little bit, it can not completely eliminate them. Our method produces the most clean and ghost-free HDRIs even for severe local movement regions.

To further evaluate our method, we compared the results of our method with those of Gallo *et. al.* [8]. Fig. 8 and 9 show the comparison of ours with [8]. Two input sequences in Fig. 8 and 9 are from [8]. The standard method [3] severely suffers from ghost artifacts. Although [8] produces good results, it suffers from blending artifacts around block boundaries. On the contrary, our method produces more natural and clean HDRI with less color artifacts.

(a)   (b)   (c)   (d)   (e)

(f) Standard [3]   (g) Gallo *et. al.* [8]   (h) Proposed method

(i)   (j)   (k)

(l)   (m)   (n)

Fig. 9. Arch sequence. (a)-(e) are input LDR images, where (c) is the reference image. (f) Result of the standard method [3]. (g) Result of [8]. (h) Result of the proposed method. (i)-(k) are the magnified views of the white rectangle regions in (g). (l)-(n) are the magnified views of the white rectangle regions in (h).

5   Conclusion

In this paper, we have proposed an effective ghost elimination method for high dynamic range imaging using multiple exposure images of a dynamic scene. The proposed method is based on generalized weighted filtering using global intensity transfer functions between different exposures and refined radiance values. Our method does not need accurate ghost detection results which often include false positives or negatives, and also does not suffer from color artifacts such as visible seams between neighboring regions.

References

1. Reinhard, E., Ward, G., Pattanaik, S., Debevec, P.: High dynamic range imaging: Acquisition, display and image-based lighting. Morgan Kaufmann, San Francisco (2005)
2. Mann, S., Picard, R.W.: Being 'undigital' with digital cameras: Extending dynmaic range by combining differently exposed pictures. Technical Report 323, M.I.T. Media Lab Perceptual Computing Section (1994)
3. Debevec, P.E., Malik, J.: Recovering high dynamic range radiance maps from photographs. In: Proc. of SIGGRAPH (1997)
4. Mitsunaga, T., Nayar, S.K.: Radiometric self calibration. In: Proc. of IEEE CVPR (1999)
5. Grossberg, M.D., Nayar, S.K.: What can be known about the radiometric response from images? In: Heyden, A., Sparr, G., Nielsen, M., Johansen, P. (eds.) ECCV 2002. LNCS, vol. 2353, pp. 189–205. Springer, Heidelberg (2002)
6. Jacobs, K., Loscos, C., Ward, G.: Automatic high-dynamic range image generation for dynamic scenes. IEEE Computer Graphics and Applications 28, 84–93 (2008)
7. Grosch, T.: Fast and robust high dynamic range image generation with camera and object movement. In: Proc. of Vision, Modeling and Visualization, VMV (2006)
8. Gallo, O., Gelfandz, N., Chenz, W.C., Tico, M., Pulli, K.: Artifact-free high dynamic range imaging. In: Proc. of IEEE ICCP (2009)
9. Raman, S., Kumar, V., Chaudhuri, S.: Blind de-ghosting for automatic multi-exposure compositing. In: Proc. of SIGGRAPH Asia Sketches (2009)
10. Khan, E., Akyuz, A., Reinhard, E.: Ghost removal in high dynamic range images. In: Proc. of IEEE ICIP (2006)
11. Pedone, M., Heikkilä, J.: Constrain propagation for ghost removal in high dynamic range images. In: Proc. of VISAPP (2008)
12. Bogoni, L.: Extending dynamic range of monochrome and color images through fusion. In: Proc. of IEEE ICPR (2000)
13. Kang, S.B., Uyttendaele, M., Winder, S., Szeliski, R.: High dynamic range video. In: Proc. of SIGGRAPH (2003)
14. Boykov, Y., Veksler, O., Zabih, R.: Fast approximate energy minimization via graph cuts. IEEE Trans. PAMI 23, 1222–1239 (2001)
15. Brown, M., Lowe, D.G.: Automatic panoramic image stitching using invariant features. Int'l J. Computer Vision 74, 59–73 (2007)
16. Fischler, M.A., Bolles, R.C.: Random sample consensus: A paradigm for model fitting with applications to image analysis and automated cartography. Comm. of the ACM 24, 381–395 (1981)

17. Kim, S.J., Pollefeys, M.: Robust radiometric calibration and vignetting correction. IEEE Trans. PAMI 30, 562–576 (2008)
18. Tomasi, C., Manduchi, R.: Bilateral filtering for gray and color images. In: Proc. of IEEE ICCV (1998)
19. Fattal, R., Lischinski, D., Werman, M.: Gradient domain high dynamic range compression. In: Proc. of SIGGRAPH (2002)
20. Reinhard, E., Stark, M., Shirley, P., Ferwerda, J.: Photographic tone reproduction for digital images. In: Proc. of SIGGRAPH (2002)
21. Photomatix, `http://www.hdrsoft.com/`